Accepted Manuscript

Loading paths for an elastic rod in contact with a flat inclined surface

V.G.A. Goss, R. Chaouki

Please cite this article as: V.G.A. Goss, R. Chaouki, Loading paths for an elastic rod in contact with a flat inclined surface, *International Journal of Solids and Structures* (2016), doi: 10.1016/j.ijsolstr.2016.02.042

LOADING PATHS FOR AN ELASTIC ROD IN CONTACT WITH A FLAT INCLINED SURFACE

GOSS, V.G.A. AND CHAOUKI, R.

LONDON SOUTH BANK UNIVERSITY

ABSTRACT. Abstract: This paper computes stationary profiles of an isotropic, homogeneous, linearly elastic rod with its endpoint locations and tangents specified. One end of the rod is clamped and the other end makes contact with a flat, rigid, impenetrable surface, which is displaced towards the clamped end. This boundary value problem has applications to biomechanical sensory devices such as mammal whiskers. The paper gives exact analytical solutions to the boundary value problem, embracing the planar equilibrium configurations for both point contact and line contact with the wall. Plots of loading paths for different inclinations of the wall provide an insight into the force-displacement relationship appertaining to real world slender rods under this type of loading. This report is complemented by data obtained from corresponding experimental studies which shed light on the differences between the model, which is based on the mathematical theory of elasticity, and the mechanics of real world long slender bodies, such as mammalian vibrissal systems.

Keywords: elastica, whiskers, rod experiments, clamp-free rod

1. Introduction

The mechanics of a long elastic rod or bar that is clamped at one end and has a load applied at the other end arises in many areas of structural engineering; for example, it finds wide application in relation to the critical load that a strut or column can sustain prior to buckling, i.e., 'Euler Buckling'. It additionally arises within the context of biomechanics. For example, animal whiskers and antennae can be characterised as long, slender, flexible rods, which are fixed at one end whilst the other end is free to undergo large deflections under applied axial loadings, see Miersch et al. (2011), Birdwell et al. (2007), and Lungarella et al. (2002). In the case of certain mammals, for example rats, that load-deflection relationship provides information about their surroundings, i.e., the whisker is a sensory device, connected to its neurological system. That form of tactile sensing has attracted considerable interest from researchers in robotics and neuroscience, see for example Solomon and Hartmann (2006) and Mitchinson and Prescott (2013). If pressed further against a surface, a section of the whisker tends to establish line contact with the surface, providing further information on the shapes and textures of objects, see Dehnhardt (1994). Similar line contact problems arise in the mechanics of peeling flexible adherends and have been studied by Majidi et al. (2005). The problem of an extensible rod peeled off a flat sticky surface is the focus of a study by He et al. (2013), whilst Wu et al. (2016) consider the adhesion of the Tokay gecko, a creature whose remarkable climbing abilities are attributable to its sticky feet.

The load-deflection relationship in those point contact and line contact problems depends on properties of the rod, including its flexural rigidity, its mass per unit length, its extensibility and its intrinsic curvature. Furthermore, all of those aforementioned properties may vary with length and may additionally depend on the orientation of the rod due to anisotropy. Studies on rats, such as those by Towal et al. (2011) and Voges et al. (2012), show that taper is important and has certain biomechanical advantages. Kulikov (2013) has additionally found similar advantages in Russian Desman whiskers, and Ginter (2012) in pinniped whiskers. In one study, by Towal et al. (2011), the geometric configuration of a whisker is modelled as a parabola. Birdwell et al. (2007) include initial curvature and taper, but their model involves a linearisation of the exact expression for curvature, which strictly applies only to small deflections of a whisker. However, in formulating models that aim to provide insight into the mechanics of whiskers, it is convenient to establish a benchmark model against which the effects of initial curvature, taper, weight and so forth can be interpreted. In the mathematical theory of elasticity, the elastica

model assumes that the internal bending moment of an unshearable, inextensible rod is linearly proportional to its curvature, see Antman (2005). Since the elastica involves the exact (nonlinear) expression for curvature it applies to both large and small deflections. It establishes the basis for studies of whiskers by Clements and Rahn (2006). However, the authors do not represent the problem as a boundary value problem, nor do they solve the equations analytically.

This paper applies the elastica model, formulated as a boundary value problem, to the mechanics of both point and line contact. The rod/whisker is assumed to be isotropic and homogeneous, i.e., constant elastic stiffness along its length. Given that stiffness is more important than weight, the latter is ignored. Additionally, the rod is assumed to be inextensible and straight in its natural unstressed configuration.

Regarding the boundary conditions, we examine the equilibrium of a rod/whisker that has one end fixed (in the mammal's face) and the free end deflects upon contact with an inclined wall that is displaced towards the fixed end such that it compresses the rod/whisker. The problem of determining the configuration of a rod in point contact with an inclined load has been studied before, for example by Frish-Fay (1962) and Navaee and Elling (1992). The analysis presented here unifies the mechanics of point contact with line contact. It additionally covers a range of angles of inclination of the wall, from the vertical to the horizontal. It presents exact analytical solutions and accompanying plots that illustrate the relationship between the displacement of the wall and the corresponding compressive force exerted on the rod. The analysis is complemented by data from experiments on slender, flexible nickel-titanium rods, which shed light upon issues arising with respect to the behaviour of similar rod-like structures, such as whiskers.

The paper is set out as follows: The next section specifies the experimental set-up, the physical boundary conditions and the parametrisation of the rods used in the experiments. In the section after that, the mathematical model is expressed as a dimensionless system of six first-order nonlinear ordinary differential equations. That is followed by a full solution to the boundary value problem, involving Jacobian elliptic integrals (refer to Abramowitz and Stegun (1966) for information on those integrals and the associated elliptic functions). The penultimate section presents force-displacement loading paths of experimental data together with those predicted by elastica theory. The paper ends with a discussion of its findings within the context of further studies on whiskers and real-world problems generally.

2. Formulation of the Boundary Value Problem

Formulated during the eighteenth century by Euler and Bernoulli, the elastica is an established model for the large deflections of long slender rods; see Levien (2008) and Goss (2009) for historical perspectives. Consequently, the formulation of the boundary value problem set out in this paper follows a well trodden path, but we mention here Frish-Fay (1962) and Batista (2013) where we find related formulations, and the constrained problems considered in Plaut et al. (1999) and Domokos et al. (1997).

Nickel-titanium alloy rods of circular cross-section with radius 0.5mm and lengths varying from 300 to 500mm were selected for the experiments. We assume, with good justification, that the rods are inextensible, unshearable, isotropic and homogeneous. Each rod has length L and is parameterised by the independent arc-length variable S, where $0 \leq S \leq L$. In its unstressed condition the rod lies straight, i.e., it has no intrinsic curvature. That straight state is the reference state from which all experiments begin. It also marks out the X axis, i.e., in its natural state the rod lies along the X axis.

The rod's bent form is planar. Its configuration is specified by the coordinates $X(S)$, $Y(S)$ and an angle $\psi(S)$, measured anticlockwise from the X axis, see Fig. 1, with

$$\frac{dX}{dS} = \cos \psi, \tag{1}$$

$$\frac{dY}{dS} = \sin \psi. \tag{2}$$

The curvature Γ of the rod is expressed in terms of the change in slope:

$$\frac{d\psi}{dS} = \Gamma. \tag{3}$$

In an experiment one end of the rod, designated $S = 0$, is fixed at zero in a chuck such that its position $X(0)$ and $Y(0)$ and its slope $\psi(0)$ are fixed throughout the experiment. Those boundary conditions can be expressed as

$$X(0) = 0, \tag{4}$$

$$Y(0) = 0, \tag{5}$$

$$\psi(0) = 0. \tag{6}$$

An experiment proceeds by displacing a rigid plane surface, referred to as a 'wall', along the X axis from $S = L$ towards $S = 0$, by amount D, as shown in Fig. 1. The wall is
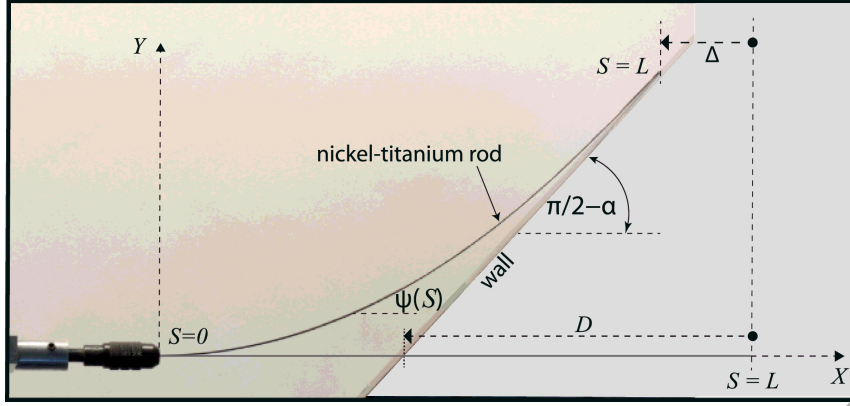
FIGURE 1. Photograph of a 1 mm diameter nickel titanium elastic rod of length 300mm clamped in a chuck at one end ($S = 0$) and deflecting against a wall at the other end ($S = L$). Note the distinction between D and Δ: In an experiment, the wall is displaced along the X axis by amount D, whereas Δ is the 'end shortening', i.e., the amount by which the tip of the rod is displaced. In the case of $\alpha = 0$ the wall is vertical and $D = \Delta$.

oriented to the X axis at an angle $\pi/2 - \alpha$, where $0 \leq \alpha \leq \frac{\pi}{2}$. We assume that friction between the wall and the rod is negligible. As D increases, the tip of the rod ($S = L$) is in point contact with the wall and deflects upwards along the wall until a point is reached whereby the tangent at the tip is parallel with the wall, i.e., $\psi(L) = \pi/2 - \alpha$. That occurs at a value of D denoted D_c. Upon further increases in displacement of the wall, $D > D_c$, the free end of the rod slides further up the wall, such that a section of rod, of length B, is in line contact with the wall. The remaining 'free' section of rod is of length $L - B$. The computation of D is with respect to that free length, as follows:

$$D = L - X(L) + Y(L)\tan\alpha, \quad \text{for point contact,} \tag{7}$$

$$D = L - X(L - B) + Y(L - B)\tan\alpha, \quad \text{for line contact.} \tag{8}$$

That set-up involves the following boundary conditions:

$$X(L) = L - \Delta, \quad \text{for} \quad D < D_c. \tag{9}$$

$$X(L - B) = L - \Delta, \quad \text{for} \quad D > D_c. \tag{10}$$

where Δ is the 'end shortening' measured to the point of first contact with the wall, i.e., for $D < D_c$ it is the amount of horizontal displacement of the tip of the rod $S = L$, and for $D > D_c$, Δ it is the horizontal displacement of the point $S = L - B$.

During an experiment, the end of the free section of the rod is in contact with the wall. The curvature (Γ) of that free section of bent rod does not change sign along its length. However, since no external bending moments are applied at the point of contact with the wall, the curvature at that point is zero and the the following holds:

$$\Gamma(L) \;=\; 0, \quad \text{for} \quad D < D_c, \tag{11}$$

$$\Gamma(L - B) \;=\; 0 \quad \text{for} \quad D > D_c, \tag{12}$$

Assuming external moments and forces, e.g., weight, are negligible, the loads acting on each element of the rod can be decomposed into a compressive force with magnitude denoted T, acting parallel with the X axis and in the negative direction, plus a force acting along the Y axis in the positive direction, with magnitude denoted N. There is also a bending moment, which acts anti-clockwise about an axis normal to the X, Y plane, of magnitude M. The forces N and $-T$ can be expressed in terms of R, the force acting normal to the wall, where $R^2 = N^2 + (-T)^2$, see Fig. 2. From consideration of the equilibrium of the rod under those loads, it follows that

$$\frac{dT}{dS} \;=\; 0, \tag{13}$$

$$\frac{dN}{dS} \;=\; 0, \tag{14}$$

$$\frac{dM}{dS} \;=\; T \sin\psi - N \cos\psi. \tag{15}$$

The magnitude of T depends on α, such that

$$T = -R\cos\alpha, \quad \text{for} \quad 0 < S < L \quad \text{if} \quad D < D_c \quad \text{and for} \quad 0 < S < L - B \quad \text{if} \quad D > D_c. \tag{16}$$

Note that in the experiments all the measurements of T are in the range from -0.5 to -1N. The transducers used to measure the forces have a sensitivity of ± 0.0001N and the experimental data represent the mean values for three consecutive experiments.

Finally, the mathematical model is completed by a linear constitutive relation which connects Eq. (3) with Eq. (15):
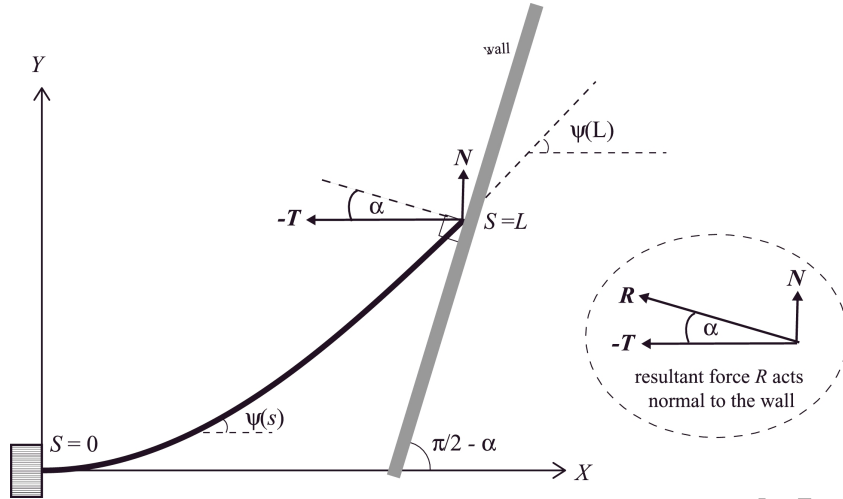
$$M = EI\Gamma, \tag{17}$$

FIGURE 2. A generic configuration of the rod involving point contact with the wall, i.e., $D < D_c$. Note that T is a compressive force and corresponds to the component of R measured in an experiment.

where E is the modulus of elasticity (N/m^2) and I is the second moment of area of the cross section (m^4). The product EI is the flexural rigidity of the material. The value of EI for the nickel titanium rods used in the experiments was determined using the deflection formula for a simple cantilever subjected to an end point load F acting normal to the rod axis:

$$y_L = \frac{FL^3}{3EI} \tag{18}$$

where y_L is the deflection measured at the free end of the rod. Tests found that $EI = 0.0027$ Nm^2, from which it follows that $E = 55.00$ GNm^{-2}. These values correlate well with the range $32 - 60$ GNm^{-2} reported in Goss et al (2005).

3. Nondimensional form of equations

3.1. **The ODEs.** For the purposes of analysis it is convenient to non-dimensionalise the variables:

$$s = \frac{S}{L},\, x = \frac{X}{L},\, y = \frac{Y}{L},\, d = \frac{D}{L},\, \delta = \frac{\Delta}{L},\, b = \frac{B}{L},\, \kappa = L\Gamma,\, r = \frac{RL^2}{EI},\, t = \frac{TL^2}{EI},\, n = \frac{NL^2}{EI},\, m = \frac{ML}{EI}. \tag{19}$$

Accordingly, in non-dimensional form, the ordinary differential equations (ODEs) Eqs. (1)–(3) and Eqs.(13)–(15), become:

$$\dot{\psi} \;=\; \kappa, \tag{20}$$

$$\dot{\kappa} \;=\; -r\cos\alpha\sin\psi - r\sin\alpha\cos\psi, \tag{21}$$

$$\dot{y} \;=\; \sin\psi, \tag{22}$$

$$\dot{x} \;=\; \cos\psi, \tag{23}$$

$$\dot{r} \;=\; 0, \tag{24}$$

where the dot denotes differentiation with respect to the scaled arc length s, where $0 \leq s \leq 1$. The first thing to note in Eqs. (20)-(24), is that the analysis is conducted in terms of r, rather than t and n, and that it follows from Eq. (24) that r is conserved, i.e., at each point along the rod, for any bent state, the value of r is constant. We can express t and n in terms of r, as follows:

$$t = -r\cos\alpha, \quad n = r\sin\alpha, \quad r^2 = t^2 + n^2. \tag{25}$$

Note that the rod is under compression and t takes negative values.

3.2. **Boundary conditions at the clamped end.** In non-dimensional form, the boundary conditions at the clamped end, i.e., Eqs. (4)-(6), are as follows:

$$x(0) \;=\; 0, \tag{26}$$

$$y(0) \;=\; 0, \tag{27}$$

$$\psi(0) \;=\; 0. \tag{28}$$

Next, we specify the conditions at the other end of the rod in two parts. First, for conditions of point contact, whereby $d < d_c$. Second, for conditions whereby a section of the rod is in line contact and $d > d_c$. Fig. 3 illustrates the loading sequence for three different configurations as d increases through d_c.

3.3. **Boundary conditions if $d < d_c$.** The non-dimensional form of Eq. (7) is

$$d = 1 - x(1) + y(1)\tan\alpha, \quad \text{for} \quad d < d_c. \tag{29}$$

The boundary conditions corresponding to Eq. (9) and Eq. (11) are

$$x(1) \quad = \quad 1 - \delta, \tag{30}$$

$$\kappa(1) \quad = \quad 0, \tag{31}$$

3.4. **Boundary conditions if $d > d_c$.** Following Plaut et al. (1999), we define l as the length of that section of rod not in contact with the surface, where $l = 1 - b$. Consequently, the non-dimensional form of Eq. (8) is

$$d = 1 - x(l) + y(l) \tan \alpha, \quad \text{for} \quad d > d_c, \tag{32}$$

and the boundary conditions corresponding to Eq. (10) and Eq. (12) are specified at $s = l$,

$$x(l) \quad = \quad 1 - \delta, \tag{33}$$

$$\kappa(l) \quad = \quad 0, \tag{34}$$

4. Solutions

The system of first order ODEs, i.e., Eqs. (20)-(24), together with the boundary conditions Eqs. (26)-(28) and either Eqs. (30)-(31) or Eqs. (33)-(34), form a well posed system. That system is suitable for numerical integration. However, the approach here is to integrate the nonlinear ODEs in closed form. Problems of this type are treated by Frisch-Fay (1962) and Batista (2013).

Load-displacement loading paths, i.e., plots of t versus d, offer a straightforward forum for comparing experimental data with predictions by the theory. That requires expressions for d and t in terms of α, the angle of inclination of the wall. Whilst the appropriate dependent variable in Eqs. (20)-(24), is the slope ψ, it is convenient to introduce a new variable θ which sums the contribution of both angles,

$$\theta = \psi + \alpha. \tag{35}$$

At the critical value of end displacement, denoted d_c, the free end of the rod is deflected such that the tangent at that end is parallel to the surface of the rigid wall, and for $d > d_c$ that condition holds for the section of rod, of length b, i.e.,

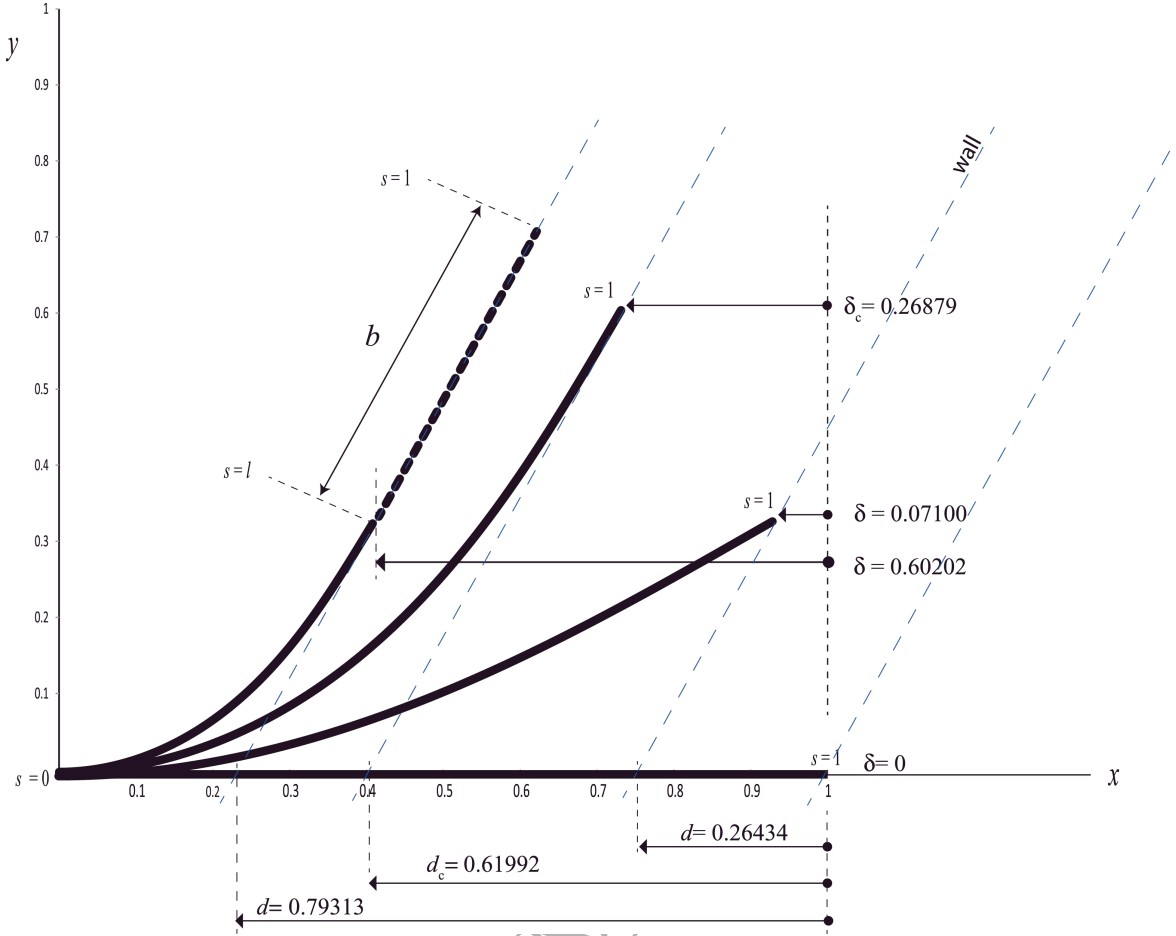$$\psi(1 - b) = \pi/2 - \alpha, \quad \text{for} \quad b > 0. \tag{36}$$

FIGURE 3. Three non-dimensional configurations (plus the straight rod) for the case $\alpha = \pi/6$. The three configurations are for $d < d_c$, d_c and $d > d_c$. In the last case, a section of the rod of length $b = 0.455722$ is in line contact with the wall. Note that d is the distance the wall moves along the x axis, whilst δ is the distance to the point where the rod first makes contact with the wall, also referred to as 'end shortening'.

We proceed by deriving equations for r, $x(1)$, $y(1)$ that can be used with the equation for d, Eq. (29), to compute t-d loading paths.

4.1. **Curvature, length and the force.** In general, and in contrast to the force, the bending moment, and therefore the curvature, varies along the length of the rod. To determine that variation we use Eq. (20) with Eq. (21) and Eq. (35) to give

$$\kappa d\kappa = (-r \cos \alpha \sin \psi - r \sin \alpha \cos \psi) \, d\psi = -r \sin \theta d\theta. \tag{37}$$

Integrating Eq. (37) and noting that $\theta(1) = \psi(1) + \alpha$, it follows from Eq. (31) that

$$\kappa = \sqrt{2r}\sqrt{\cos \theta - \cos \theta(1)}, \tag{38}$$

where the positive sign in Eq. (38) has been chosen to concur with the curvature observed in the experiments, see Fig. 1. We proceed by deriving an explicit equation for the length of the rod, in terms of r, α and $\psi(1)$. Using Eq. (38) in Eq. (20) we find

$$ds = \int_\alpha^{\theta(1)} \frac{d\theta}{\sqrt{2r}\sqrt{\cos\theta - \cos\theta(1)}} = \int_\alpha^{\theta(1)} \frac{1}{2\sqrt{r}} \frac{d\theta}{\sqrt{\sin^2 \frac{\theta(1)}{2} - \sin^2 \frac{\theta}{2}}} \qquad (39)$$

and splitting the integral on the right hand side into two parts,

$$ds = -\int_0^\alpha \frac{1}{2\sqrt{r}} \frac{d\theta}{\sqrt{\sin^2 \frac{\theta(1)}{2} - \sin^2 \frac{\theta}{2}}} + \int_0^{\theta(1)} \frac{1}{2\sqrt{r}} \frac{d\theta}{\sqrt{\sin^2 \frac{\theta(1)}{2} - \sin^2 \frac{\theta}{2}}}. \qquad (40)$$

It is pertinent at this point to introduce the elliptic modulus p and elliptic amplitude ϕ:

$$p = \sin\frac{\theta(1)}{2}, \quad p\,\sin\phi = \sin\frac{\theta}{2}, \quad 0 \le \phi \le \pi/2. \qquad (41)$$

Combining Eq. (40) with Eq. (41) we obtain, after some manipulation:

$$\int_0^s ds = s = \int_0^{\phi_b} \frac{1}{\sqrt{r}} \frac{d\phi}{\sqrt{1 - p^2 \sin^2\phi}} - \int_0^{\phi_a} \frac{1}{\sqrt{r}} \frac{d\phi}{\sqrt{1 - p^2 \sin^2\phi}} = \frac{1}{\sqrt{r}} \left\{ F(\phi_b|p^2) - F(\phi_a|p^2) \right\}, \qquad (42)$$

where F is an incomplete elliptic integral of the first kind and the elliptic amplitudes ϕ_a and ϕ_b are respectively as follows:

$$\phi_a = \sin^{-1}\left[\frac{\sin\alpha/2}{p}\right], \qquad \phi_b = \sin^{-1}\left[\frac{\sin\theta/2}{p}\right]. \qquad (43)$$

The total length of the rod is obtained by setting $\psi = \psi(1)$, so that $\phi_b = \pi/2$ and Eq. (42) becomes

$$\int_0^1 ds = 1 = \frac{1}{\sqrt{r}} \left\{ K(p^2) - F(\phi_a|p^2) \right\}, \qquad (44)$$

where K is a complete elliptic integral of the first kind.

For given values of α and p, Eq. (44) can be used to find r and hence the 'rig force', $t = -r\cos\alpha$,

$$t = -r\cos\alpha = -\left(K(p^2) - F(\phi_a|p^2)\right)^2 \cos\alpha, \quad \text{for} \quad d < d_c. \qquad (45)$$

Note that when $\alpha = 0$ the elliptic amplitude ϕ_a vanishes and $r = (K(p^2))^2$, whereby, for $p = 0$, we obtain

$$t = -t_E = -\frac{\pi^2}{4}, \tag{46}$$

which is the Euler buckling load. We add here that linearisation of the second order differential equation formed by combining Eq. (20) with Eq. (21) together with the boundary conditions Eqs. (28) and (31) shows that

$$t = -t_{Ek} = -\left(k + \frac{1}{2}\right)^2 \pi^2, \qquad k = 0, 1, 2, 3... \tag{47}$$

where the whole number k indicates a buckling mode; $k = 0$ corresponds to Eq (46) the first mode, $k = 1$ to the second mode and so forth.

Note that Eq. (45) can be used for $d < d_c$. For $d > d_c$, Eq. (36) applies and there is a section of rod, of length b, which is in line contact with the wall (see Fig. 1). Consequently, the integration starts at $s = 0$ and ends at a point $s = l$, where l is the length of that section of rod not in line contact with the wall, and $l + b = 1$. Furthermore, whilst in general the elliptic modulus takes values $0 \leq p \leq 1$, in this boundary value problem the upper limit is $p = \frac{\sqrt{2}}{2}$. It follows, that for $d > d_c$, the force t is given by:

$$t = -r\cos\alpha = -\frac{\left(K(\frac{1}{2}) - F(\phi_a|\frac{1}{2})\right)^2}{(1-b)^2}\cos\alpha, \quad \text{for} \quad d > d_c. \tag{48}$$

4.2. **The shape.** The shape of the rod is obtained from integration of Eq. (22) and Eq. (23). From the former we have

$$dy = \sin\psi ds = \sin(\theta - \alpha)\, ds \longrightarrow dy = \frac{1}{\sqrt{r}}\frac{\sin(\theta - \alpha)d\phi}{\sqrt{1 - p^2\sin^2\phi}}.$$

Applying trigonometric identities and using Eq. (41), we find that $\cos\frac{\theta}{2} = \sqrt{1 - p^2\sin^2\phi}$, and therefore $\sin\theta = 2p\sin\phi\sqrt{1 - p^2\sin^2\phi}$. Consequently, we obtain

$$dy = \frac{2p}{\sqrt{r}}\cos\alpha\sin\phi\, d\phi - \frac{1}{\sqrt{r}}\sin\alpha\left[\frac{d\phi}{\sqrt{1 - p^2\sin^2\phi}} - \frac{2p^2\sin^2\phi\, d\phi}{\sqrt{1 - p^2\sin^2\phi}}\right] \tag{49}$$

and integrating with limits ϕ_b and ϕ_a:

$$y = \frac{2p}{\sqrt{r}}\cos\alpha\left(\cos\phi_a - \cos\phi_b\right) - \frac{1}{\sqrt{r}}\sin\alpha\left[\mathrm{F}\left(\phi_a|p^2\right) - \mathrm{F}\left(\phi_b|p^2\right) + 2\mathrm{E}\left(\phi_b|p^2\right) - 2\mathrm{E}\left(\phi_a|p^2\right)\right]. \tag{50}$$

From Eq. (23) we have

$$dx = \cos\theta\, ds = \frac{1}{\sqrt{r}}\frac{\cos\theta\, d\phi}{\sqrt{1 - p^2\sin^2\phi}},$$

using $\cos\theta \equiv 1 - 2\sin^2\frac{\theta}{2} = 1 - 2p^2\sin^2\phi$, and following the procedure used to derive an expression for y set out above, we integrate and find that

$$x = \frac{1}{\sqrt{r}}\left\{\cos\alpha\left[\mathrm{F}\left(\phi_a|p^2\right) - \mathrm{F}\left(\phi_b|p^2\right) + 2\mathrm{E}\left(\phi_b|p^2\right) - 2\mathrm{E}\left(\phi_a|p^2\right)\right] + 2p\sin\alpha\left(\cos\phi_a - \cos\phi_b\right)\right\} \tag{51}$$

where $\mathrm{E}\left(\phi|p^2\right)$ is the incomplete elliptic integral of the second kind. The two equations Eq. (51) and Eq. (50) describe the shape of the bent rod.

Computation of d involves $y(1)$ and $x(1)$, (see Eq. (29) and Eq. (32)). These are obtained by setting $\psi = \psi(1)$ in Eq. (43) such that $\phi_b = \pi/2$ giving

$$y(1) = \frac{2p}{\sqrt{r}}\cos\alpha\cos\phi_a - \frac{1}{\sqrt{r}}\sin\alpha\left[\mathrm{F}\left(\phi_a|p^2\right) - \mathrm{K}\left(p^2\right) + 2\mathrm{E}\left(p^2\right) - 2\mathrm{E}\left(\phi_a|p^2\right)\right] \tag{52}$$

and

$$x(1) = \frac{1}{\sqrt{r}}\left\{\cos\alpha\left[\mathrm{F}\left(\phi_a|p^2\right) - \mathrm{K}\left(p^2\right) + 2\mathrm{E}\left(p^2\right) - 2\mathrm{E}\left(\phi_a|p^2\right)\right] + 2p\sin\alpha\cos\phi_a\right\}. \tag{53}$$

Note that for the case $\alpha = 0$, Eq. (52) and Eq. (53) reduce respectively to

$$y(1) = \frac{2p}{\sqrt{r}}, \quad x(1) = \frac{1}{\sqrt{r}}\left[2\mathrm{E}\left(p^2\right) - \mathrm{K}\left(p^2\right)\right]. \tag{54}$$

5. Results

For different values of α, a set of loading paths is shown in Fig. 4. They are obtained using Eq. (29) with Eq. (45) for $d < d_c$, and Eq. (32) with Eq. (48) for $d > d_c$. The curve of values of d_c in that figure is obtained by setting $p = \frac{\sqrt{2}}{2}$ in Eq. (29) and Eq. (45). Some values of d_c for corresponding α are given in Table 1. Note that for the limit $\alpha \to \frac{\pi}{2}, d_c \to \frac{2}{3}$.

Loading paths for particular values of α together with corresponding data from experiments are shown in Figs. 5-9. Note that the t-d plots in all those figures are normalised by dividing t by t_E, the Euler buckling load given in Eq. (46). Inspection of those figures shows good correlation between theory and experimental data.

TABLE 1

α	d_c	t_c
$5\pi/12$	0.664038	-0.055049
$\pi/3$	0.655937	-0.214173
$\pi/4$	0.641672	-0.459711
$\pi/6$	0.619918	-0.763555
0	0.543053	-1.393204

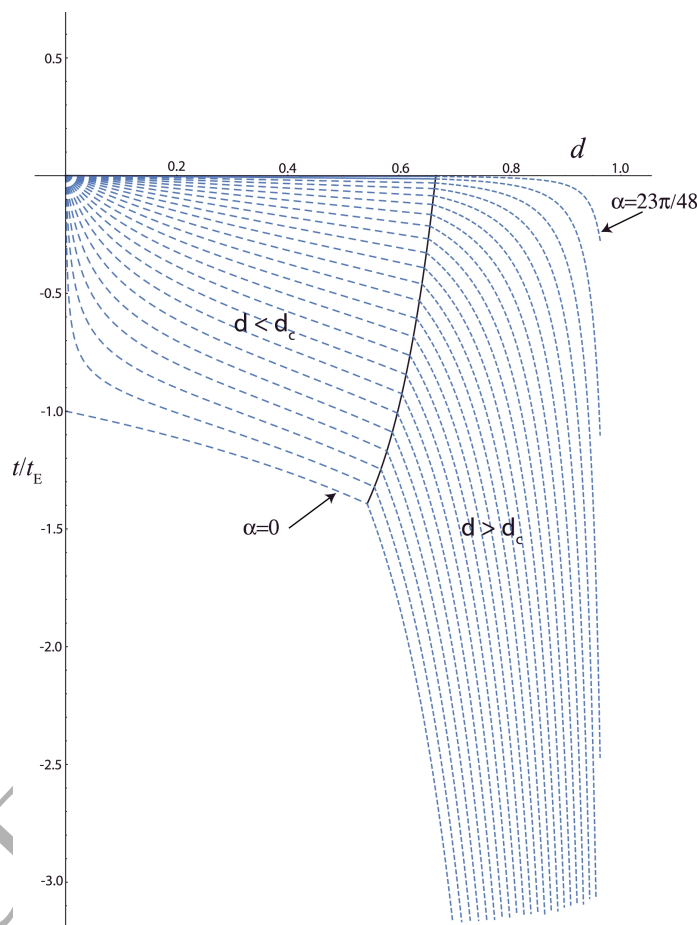

FIGURE 4. Theoretical loading paths for a range of values of α, in steps of $\alpha = \frac{\pi}{48}$, including the curve for d_c (solid). Each t-d loading path involves a region in which the whole rod is in point contact ($d < d_c$) and a region in which part of the rod is in line contact ($d > d_c$).

6. DISCUSSION

One of the challenges in research involving theory and experiments is to eliminate experimental error and close the gap between the experiment and theory. Inevitably, the experimental set-up includes unavoidable imperfections. One significant practical problem
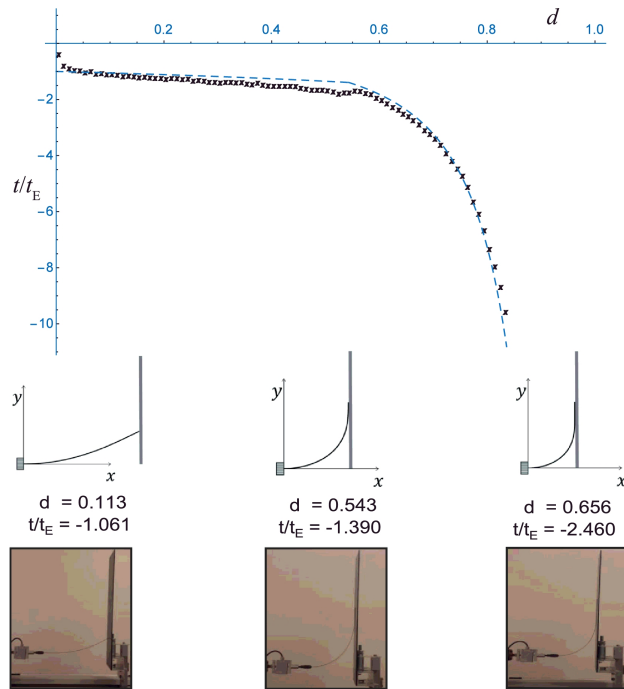
FIGURE 5. The loading path for $\alpha = 0$, i.e., an axially applied load. The theory shows a primary bifurcation at $\frac{4TL^2}{\pi^2 EI} = -1$, corresponding to Eq. (46). However, the experimental loading path 'rounds off' that bifurcation due to experimental 'imperfections' (see the Discussion). Line contact occurs at $(d_c, t_c) = (0.543, -1.390)$.
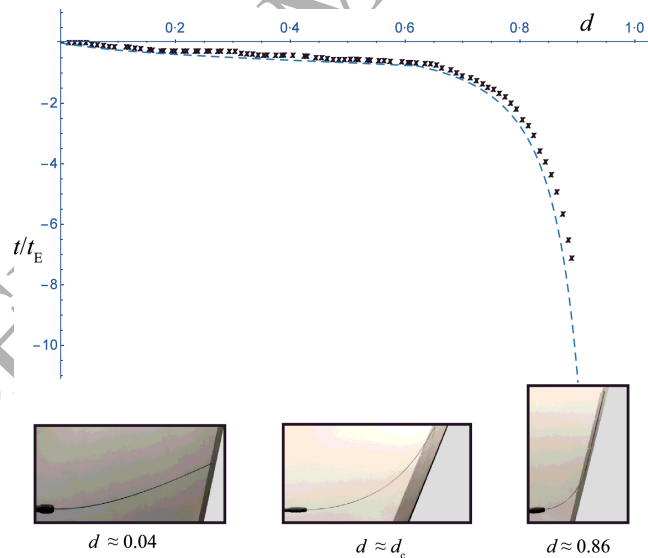

FIGURE 6. Experimental and theoretical loading paths for $\alpha = \frac{\pi}{6}$, showing three photographs from the experiment, where the corresponding theory predicts $(d, t/t_E) = (0.037, -0.114), (0.620, -0.764), (0.861, -5.724)$.

is the presence of friction. Whilst measures were taken to reduce friction, for example the surface of the wall was lubricated, close inspection of the experimental data reveals 'stick slip' phenomena. This is more evident for $d < d_c$, i.e., when the tip of the rod is in
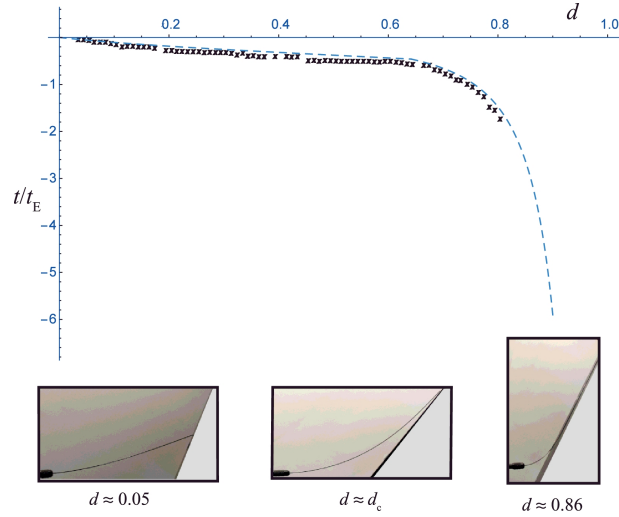
FIGURE 7. Experimental and theoretical loading paths for $\alpha = \frac{\pi}{4}$, showing three photographs from the experiment, where the corresponding theory predicts $(d, t/t_E) = (0.05, -0.055), (0.642, -0.460), (0.868, -3.381)$.
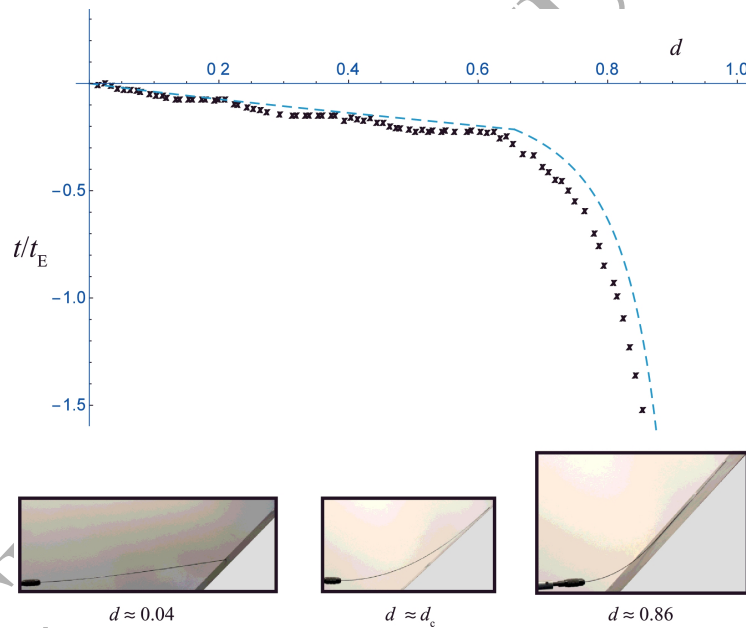

FIGURE 8. Experimental and theoretical loading paths for $\alpha = \frac{\pi}{3}$, showing three photographs from the experiment, where the corresponding theory predicts $(d, t/t_E) = (0.043, -0.0017), (0.656, -0.214), (0.864, -1.390)$.

point contact with the wall. For $d > d_c$, when line contact is inaugurated, the rod slides across the surface and the coefficient of friction between the surfaces is kinetic, rather than static. Studies by Shultz et al. (2005) suggest that friction assists rats in gathering information on surface textures. The steep gradient displayed in the t-d plots for $d > d_c$ suggests that the distinction between point and line contact may play a significant role in how animals use whiskers to gather information about their surroundings.
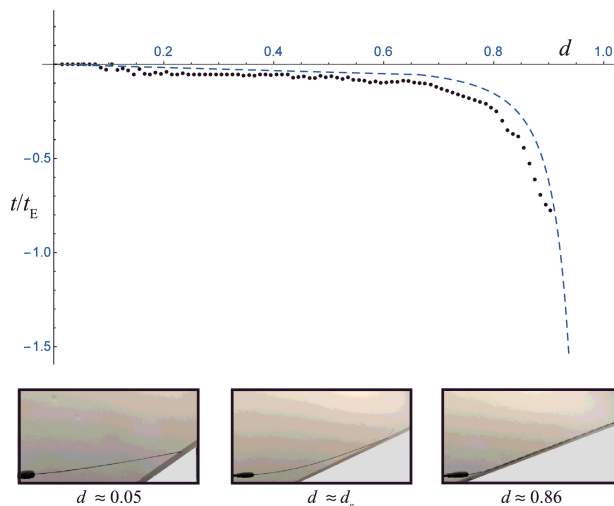
FIGURE 9. Experimental and theoretical loading paths for $\alpha = \frac{5\pi}{12}$, showing three photographs from the experiment, where the corresponding theory predicts $(d, t/t_E) = (0.051, -0.0044), (0.664, -0.055), (0.864, -0.334)$.
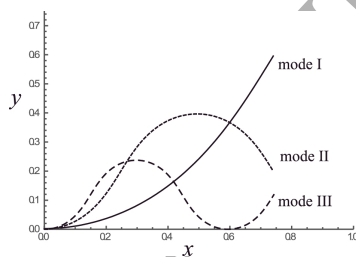

FIGURE 10. Three different configurations corresponding to the first three buckling modes for $\alpha = 0$ and $(d, t/t_E) = (0.259, -1.152), (0.259, -10.366), (0.259, -28.793)$, for Modes I, II and III respectively.

Due to unavailability of rats and appropriate facilities for conducting experiments on whiskers, the experimentation in this study is restricted to nickel-titanium rods. However, reports of experiments on whiskers are given in Quist et al. (2008). Overall, the good qualitative and quantitative correlation between the data obtained from our experiments with that predicted by the theory shows that the elastica provides a close description of the mechanics of a bent nickel-titanium rod. That applicability has been shown elsewhere, Goss et al (2005). Of course these 'engineered rods', unlike 'biological rods', are manufactured under controlled specifications and closely approximate the assumptions of isotropy, homogeneity and zero initial curvature. However, in the case of real-world biological 'rods', such as whiskers, those assumptions are no longer valid. Whiskers are generically not only anisotropic, they also have weight, and many whiskers have initial curvature and may additionally have intrinsic tortuosity. With reference to the planar

elastica, such attributes can be considered imperfections. The $t - d$ loading paths presented here shed light on how those imperfections manifest. For example, inspection of the experimental data in Fig. 5 suggests that no bifurcation occurs for the case $\alpha = 0$. That mismatch can be attributed to both the sagging effect of the rod's weight, which is not included in the mathematical model, and the fact that even a tiny misalignment of the end force causes a correspondingly small deflection. Those can be considered small imperfections and consequently the experimental loading path shows a generic 'rounding off' of the primary bifurcation predicted by the theory. Preliminary studies indicate that inclusion of terms appertaining to taper manifests itself as an imperfection in a similar manner.

It may be observed that the theoretical loading path for $\alpha = 0$, see Fig. 4, is qualitatively different from the other cases. That is because for $\alpha = 0$ the rod is loaded by a purely axially applied force whereby buckling occurs at the critical load t_E. For $\alpha > 0$ buckling does not arise because for any small lateral component of force there is a correspondingly small deflection. It may additionally be observed that all the configurations shown in Figs. 5-9 involve rods with no inflection points. However, for $\alpha = 0$ higher buckling modes exist. They are obtained using Eq. (47), whereby $t = -r$, with corresponding values for k in Eq. (50) and Eq. (51). Fig. 10 shows three post-buckled configurations corresponding to the first three modes. An inspection of Fig. 10 indicates that for each of those configurations, for $0 < s < 1$, the number of inflection points corresponds to the value of k in Eq. (47), i.e., zero inflection points in the first mode ($k = 0$), one inflection point in second mode ($k = 1$) and so forth. The arc length between consecutive inflection points is scaled by $\sqrt{r}$ such that the total length of the rod remains equal to one. Note, it follows from Eq. (38) that inflexions are given by $\cos \theta = \cos \theta(1)$. They are equally spaced along the x axis and lie along the line of action of the end force r, see Love (1952). Whilst those modes were not observed in the experiments reported here they can be observed if a suitable constraint is deployed that suppresses primary buckling at t_E. Furthermore, although for $\alpha > 0$ the rod does not buckle, it may be possible to observe configurations corresponding to higher modes with $\alpha > 0$ by adjusting the loading sequence, i.e., start at $\alpha = 0$ with a constraint to suppress the primary mode, introduce d, and then adjust α.

The elastica is presented here as a reference point for studies on the deformation of animal whiskers. We remark here that the solutions to this boundary value problem (BVP) can be difficult to interpret, for they are expressed in terms of Jacobian elliptic

integrals which involve the elliptic modulus and the elliptic argument. Moreover, it is relatively straightforward to compute numerical solutions to this BVP and to incorporate additional terms that account for anisotropy and non-homogeneity, such that the mathematical model more closely accounts for the real-world geometric morphology of whiskers. However, by including those attributes, closed form integrability vanishes, see van der Hiejden and Yagasaki (2104). Another issue to consider is that changes in the boundary conditions yield qualitatively different solutions to the elastica equations. For example, studies by Kuznetzov and Levyakov (2002) reveal the existence of secondary bifurcations in the case of rods with both ends clamped. Furthermore, research that extends to consideration of three-dimensional configurations, involving twisted rods, requires a larger system of equations. Although that system can also be reduced to quadrature, it is considerably more difficult to interpret than the planar system presented here and additionally embraces a wider arena of complicated nonlinear phenomena (van der Heijden et al, 2003), which can be observed in experiments on twisted rods, see Goss et al. (2005). Consequently, the availability of a relatively simple closed-form solution to a nonlinear BVP, formulated within the context of the mathematical theory of elasticity, is not trivial. It establishes the planar elastica as the key reference point for studies on rod-like structures, whether they be nickel-titanium rods or rat whiskers. It is hoped that this paper demonstrates and highlights that role.

References

Abramowitz, M., Stegun, I., 1966. Handbook of Mathematical Functions. Applied Mathematics Series 55.

Antman, S., 2005. Nonlinear Problems of Elasticity 2nd ed. Springer, Dordrecht.

Batista, M., 2014. Analytical treatment of equilibrium configurations of cantilever under terminal loads using Jacobi elliptical functions. International Journal of Solids and Structures 51(13), 2308–2326.

Birdwell, J.A., Solomon, J.H., Thajchayapong, M., Taylor, M.A., Cheely, M., Towal, R.B., Conradt, J., Hartmann, M.J.Z., 2007. Biomechanical models for radial distance determination by the rat vibrissal system. Journal of Neurophysiology 98(4), 2439–2455.

Clements, T.N., Rahn, C.D., 2006. Three-dimensional contact imaging with an actuated whisker. IEEE Transactions on Robotics 22(4), 844–848.

Dehnhardt, G., 1994. Tactile size discrimination by a California sea lion (Zalophus californianus) using its mystacial vibrissae. Journal of Comparative Physiology A 175(6), 791–800.

Domokos, G., Holmes, P., Royce, B., 1997. Constrained Euler buckling. Journal of Nonlinear Science 7(3), 281–314.

Frisch-Fay, R., 1962. Flexible Bars. Butterworths, London.

Ginter Summarell, C.C., Sudeep, I., Fish, F.E., Marshall, C.D., 2015. Comparative analysis of the flexural stiffness of pinniped vibrissae. PloS one 10(7), 1–17.

Goss, V.G.A., 2009. The history of the planar elastica: Insights into mechanics and scientific method. Science and Education 18(8), 1057–1082.

Goss, V.G.A., van der Heijden, G.H.M., Thompson, J.M.T., Neukirch, S., 2005. Experiments on snap buckling, hysteresis and loop formation in twisted rods. Experimental Mechanics 45(2), 101–111.

He, L. W., Yan, S. P., Li, B. Q., Zhao ,G., Chu, J.R., 2013. Adhesion model of side contact for an extensible elastic fiber. International Journal of Solids and Structures 50(16-17), 2659-2666.

Kulikov, V. F., 2013. The structure of tactile organs of the Russian Desman (Desmana moschata L. 1758) and Their role in orientation. Doklady Biological Sciences 449(1), 99.

Kuznetsov, V.V., Levyakov, S.V., 2002. Complete solution of the stability problem for elastica of Euler's column. International Journal of Non-Linear Mechanics 37, 1003-1009.

Levien, R., 2008. The elastica: a mathematical history. Technical Report. Electrical Engineering and Computer Sciences Department, University of California, Berkeley.

Love, A,E,H., (1952). The Mathematical Theory of Elasticity 4th ed. Cambridge University Press, Cambrdige.

Lungarella, M., Hafner, V.V., Pfeifer, R., Yokoi, H., 2002. An artificial whisker sensor for robotics. Intelligent Robots and Systems, 2002. IEEE/RSJ International Conference on 3, 2931–2936.

Majidi, C.S., Groff, R. E., Fearing, R. S., 2005. Attachment of fiber array adhesive through side contact. Journal of Applied Physics 98, 103521.

Mitchinson, B., Prescott, T.J., 2013. Whisker movements reveal spatial attention: A unified computational model of active sensing control in the rat. PLOS Computational Biology 9(9), 1-16.

Navaee, S., Elling, R.E., 1992. Equilibrium configurations of cantilever beams subjected to inclined end loads. Journal of Applied Mechanics 59, 572-579.

Plaut, R.H., Suherman,S., Dillard, D.A., Williams, B.E., Watson, L.T., 1999. Deflections and buckling of a bent elastica in contact with a flat surface. International Journal of Solids and Structures. 36(8), 1209–1229.

Quist, B.W., Hartmann, M.J.Z., 2008. A two-dimensional force sensor in the millinewton range for measuring vibrissal contacts. Journal of Neuroscience Methods 172, 158-167.

Shultz, A., Solomon, J., Peshkin, M.A., Hartmann, M.J.Z., 2005. Multifunctional whisker arrays for distance detection, terrain mapping, and object feature extraction. Robotics and Automation. ICRA 2005. Proceedings of the 2005 IEEE International Conference, 2588–2593.

Solomon, J., Hartmann, M.J.Z., 2006. Robotic whiskers used to sense features. Nature 443(5), 525.

Towal, R. B., Quist, B.W., Gopal, V., Solomon, J.H., Hartmann, M.J.Z., 2011. The morphology of the rat vibrissal array: A model for quantifying spatiotemporal patterns of whisker-object contact. PLOS Computational Biology 7(4), 1–17.

van der Heijden, G.H.M., Neukirch, S., Goss, V.G.A., Thompson, J.M.T., 2003. Instability and self-contact phenomena in the writhing of clamped rods. International Journal of Mechanical Sciences 45, 161–196.

van der Heijden, G.H.M., and Yagasaki. K., 2014. Horseshoes for the nearly symmetric heavy top. Z. Angew. Math. Phys. (ZAMP) 65, 221–240.

Voges, D., Carl, K., Klauer, G.J., Uhlig, R., Schilling, C., Behn, C., Witte, H., 2012. Structural characterization of the whisker system of the rat. IEEE Sensors Journal 12(2), 332–339.

Wu, X., Wang, X., Mei, T., Sun, S., 2015. Mechanical analyses on the digital behaviour of the Tokay gecko (Gekko gecko) based on a multi-level directional adhesion model. Proceedings of the Royal Society A - Mathematical, Physical and Engineering Sciences, 471(2179), 20150085.